ACS APPLIED ENERGY MATERIALS

www.acsaem.org Article

Combined Rotating Disk Slurry Electrodeposition–Spontaneous Galvanic Displacement for Pt-M (M = Co, Ni, and Cu) Catalyst Synthesis for the Oxygen Reduction Reaction in Alkaline Media

Joesene J. Soto Pérez, Armando Peña-Duarte, Pedro Trinidad, Gerardo Quintana, Xueru Zhao, Kotaro Sasaki, Miguel José Yacamán, Rubén Mendoza-Cruz, and Carlos R. Cabrera*

Cite This: *ACS Appl. Energy Mater.* 2022, 5, 15175–15187 Read Online

ACCESS | Metrics & More | Article Recommendations | Supporting Information

ABSTRACT: Platinum-modified first-row transition-metal catalyst (M = Ni, Co, and Cu) nanoparticles on a carbon black Vulcan XC-72R (CBV) support were synthesized using rotating disk slurry electrodeposition (RoDSE) followed by spontaneous galvanic displacement (SGD) reactions. These RoDSE–SGD catalysts were evaluated for the oxygen reduction reaction (ORR) in 0.1 M KOH using rotating disk electrode techniques. The Ni and Co RoDSEs were done by using an electrochemical applied potential of −0.75 V versus the RHE and for Cu, −0.80 V versus the RHE using a CBV slurry solution containing 0.1 M $KClO_4$. These metal nanoparticles on CBV (M/CBV) catalysts were modified with a Pt precursor via a spontaneous galvanic displacement (SGD) reaction, producing a Pt-M/CBV material to catalyze the ORR in an alkaline medium. High-resolution scanning transmission electron microscopy (HR-STEM) analysis indicates that the PtM/CBV samples include M clusters and Pt single atoms. The ORR characterization measurements were done under a controlled temperature (25.0 °C) and with a mass loading of 100 $\mu g/cm^2$ on a glassy carbon (GC) rotating disk electrode at 1600 rpm. The PtCo/CBV showed the highest ORR mass activity of 0.741 A/mg_{Pt} at 0.90 V versus the reversible hydrogen electrode (RHE) compared with commercial Pt/CBV. The M/CBV RoDSE catalysts were also tested for the oxygen evolution reaction (OER), and Ni/CBV provided the lowest overpotential of 450 mV at 10 mA/cm^2_{disk} in 0.1 M KOH.

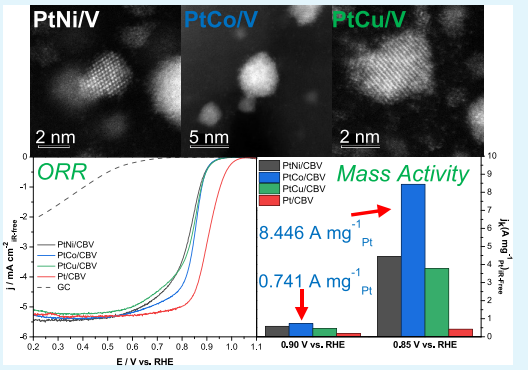

KEYWORDS: *ORR, electrodeposition, electrocatalysis, interfaces, in situ XAS, first-row transition metals, OER*

1. INTRODUCTION

The use of catalysts has paved the route to enhance renewable energy technologies, and their development for specific energy conversion reactions could provide the path to replacing fossil fuels. Among these technologies, clean hydrogen production has received recent interest[1] as seen from governments investing in energy programs such as the Hydrogen Hubs from the US Department of Energy (DOE).[2] Clean green hydrogen[3] could be obtained using an electrolyzer based on water-splitting reactions—hydrogen evolution reaction (HER) and oxygen evolution reaction (OER). The green hydrogen could be stored and used in technologies such as anion exchange membrane fuel cells (AEMFCs), which are great contenders for use in electric vehicles. In AEMFCs, the stored clean hydrogen will react with an anode catalyst for the hydrogen oxidation reaction (HOR), while at the cathode catalyst, the oxygen reduction reaction (ORR) will occur.

The initial performance of AEMFCs is close to that of already commercialized proton exchange membrane fuel cells (PEMFCs). Working in an alkaline environment enhances the ORR at the cathode. In contrast, the ORR kinetics in an acidic medium has sluggish behavior[4] and requires highly active materials—platinum group metals (PGMs)—leading to high costs and unreliable commercialization.[5] Scientific efforts to minimize PGMs used in ORR catalysts are being done to provide realistic consumable commercialization and accessibility.[6] The transition to an alkaline medium reduces or even replaces the use of a PGM catalyst. Different catalysts that are less expensive, more abundant, and durable such as metal nitrides, metal oxides, and non-precious metals can be explored in this instance.

Non-PGM–PGM alloys,[7] core–shells,[8] and non-precious metal catalysts[9] are the leading contenders to replace PGM catalysts. The combination of PGMs with a non-precious metal has been demonstrated to improve ORR performance while

Received: September 1, 2022
Accepted: November 15, 2022
Published: December 1, 2022

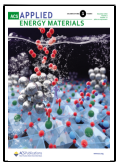

https://doi.org/10.1021/acsaem.2c02843
ACS Appl. Energy Mater. 2022, 5, 15175–15187

reducing the amount of PGMs needed. Specifically, Pt alloyed with first-row transition metals are among the most active materials—the fermi level of Pt 4d and 4f orbitals is lowered while Pt 5d orbital vacancies are increased— promoting enhanced Pt-O_2 interactions in the ORR.[10] On the other hand, for the OER, we have similar cornerbacks for commercialization; materials of precious metals such as Ir and Ru-based materials are the most studied.[11] However, non-precious metal oxides have demonstrated great activity for the OER in an alkaline medium.[12]

Different synthesis methods, such as hydrothermal, sol−gel, and chemical reduction methods, could be used to obtain ORR electrocatalysts. Electrodeposition is another alternative where the rotating disk slurry electrodeposition (RoDSE) methodology has been studied for over 10 years for catalyst preparation on unsupported carbon materials, for example, Vulcan XC-72R (CBV), single wall carbon nanotubes, reduced graphene oxide, and carbon nano-onions.[13−26] Some of the benefits of this method are the fact that no heat treatment is required and scale-up synthesis can be obtained, providing a fluent transition from the rotating disk electrode (RDE) to the membrane electrode assembly (MEA). RoDSE has been successfully used to synthesize Pt,[21] Pd,[17,24] Au,[26] Ag,[15,18] and Fe[16] nanoparticles supported on different carbon supports for energy conversion applications. However, first-row transition metals have not been thoroughly explored using RoDSE. For the ORR, Ni,[27] Co,[28,29] and Cu[30] have shown excellent activity with Pt as alloys, bimetallic metallic organic frameworks, and intermetallic structures. Recognizing the need for different catalysts for the ORR and the benefits of the RoDSE methodology, we decided to synthesize first-row transition metal nanoparticles with low Pt loading. The RoDSE methodology was used to obtain M (Ni, Co, or Cu) nanoparticles (NPs) on a CBV support via bulk electrodeposition for the OER. These M nanoparticles were further modified with a low amount of a Pt precursor via spontaneous galvanic displacement (SGD)[31] and used for the ORR. The CBV (industrially produced by Cabot Corporation) was selected for this study since it has been widely studied for fuel cell applications with an adequate surface area (ca. 250 m^2/g) and high electric conductivity (ca. 2.77 S/cm).[32−36] Using CBV as the catalyst carbon support, our combined RoDSE and SGD method resulted in PtM/V nanoparticles that had ca. 2−3% Pt *w*/*w*%—low loading—and demonstrated enhanced ORR mass activity when compared with a Pt/CBV 20% commercial catalyst.

2. RESEARCH DESIGN AND METHODS

2.1. Catalyst Synthesis. The PtM/CBV synthesis was divided into two steps. First, M was electrodeposited in a CBV slurry dispersion consisting of 50 mg of CBV and 20 mL of 0.1 M $KClO_4$ (GFS Chemicals) using the RoDSE technique where an electrochemical potential was applied to a carbon support dispersion slurry while the glassy carbon (GC) disk electrode (Pine Research Instruments) was rotated. Applied potentials of −0.75 V for Ni and Co and −0.80 V versus the reversible hydrogen electrode (RHE) for Cu were used in the RDE setup (Pine Research Instruments) at 1200 rpm in 0.1 M $KClO_4$.[21] Subsequently, the M/CBV material, synthesized by RoDSE, was modified with Pt via SGD using a 10 mM H_2PtCl_6 (Sigma-Aldrich) solution to obtain a highly dispersed and highly active PtM/CBV electrocatalyst. All the potentials presented in this work are versus an RHE.

2.2. Ni, Co, and Cu Nanoparticle Electrocatalyst Preparation via RoDSE. The RoDSE technique was done using a carbon slurry solution, which was prepared following a published procedure.[14] Briefly, the CBV slurry dispersion was prepared by placing 20 mg of CBV in 50 mL of 0.1 M $KClO_4$ and sonicating for 1 h to get a highly dispersed slurry solution. Then, the slurry was transferred to the center of a closed three-compartment electrochemical cell using an RDE setup (see Figure 1). In the middle compartment, a GC RDE

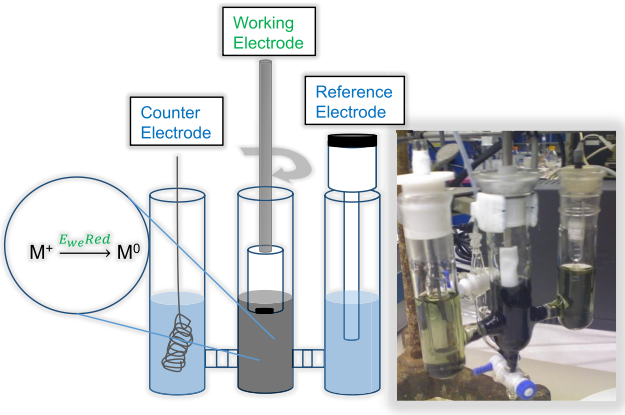

Figure 1. RoDSE methodology scheme (left) using a three-electrode electrochemical setup. Right, picture of the synthesis setup.

was used as a working electrode (WE), in the right compartment, an RHE (eDAQ) as a reference electrode (RE), and in the left compartment, a high-surface area platinum electrode (Bioanalytical Systems Inc.) as the counter electrode (CE). Subsequently, each M synthesis was done individually using an aqueous 5 mM solution of $NiCl_2$ (Sigma-Aldrich), $CoCl_2{\cdot}6H_2O$ (Sigma-Aldrich), and $CuCl_2$ (Sigma-Aldrich) in 0.1 M $KClO_4$, depending on the M precursor. A 2.00 mL aliquot of the 5 mM precursor solution was added to the middle compartment of the electrochemical cell and then purged with ultrahigh pure (UHP) N_2 gas while rotating the GC RDE at 1200 rpm. A constant N_2 purge was maintained inside the cell and the desired electrodeposition potential was applied for 1 h at −0.75 and −0.80 V versus the RHE for Cu and for Ni and Co, respectively. This electrodeposition step was repeated three additional times in intervals of 1 h for a total electrodeposition time of 4 h, and 8 mL of M precursor aqueous solution was added to 20 mg of CBV in 50 mL 0.1 M $KClO_4$ slurry solution. This solution containing M/CBV particles was filtered using a vacuum pump filter system (0.45 μm nylon membrane) and washed vigorously with deionized water. The resulting catalyst material was vacuum-dried at 40 °C for 24 h. Then, the product was recovered and grounded by hand using a quartz mortar to obtain the final powder material.

2.3. Preparation of the PtNi/CBV, PtCo/CBV, and PtCu/CBV Electrocatalysts via Spontaneous Galvanostatic Displacement. For the second step, the RoDSE M/CBV powders were used to obtain the Pt-M/CBV electrocatalysts via a spontaneous galvanostatic displacement (SGD) reaction. Briefly, 20 mg of M/CBV was placed inside a 50 mL round bottom flask with 20 mL of deionized water. This flask was heated at 95 °C using an oil bath and with a reflux setup. A mass stoichiometryc of 3 to 1 of Pt to M addition was done using a 10 mM H_2PtCl_6 aqueous solution. The calculated Pt amount was divided by a factor of 10 and added 10 times in intervals of 1 min to the bottom flask to start the SGD, and we stirred it for 2 h. The resulting PtM/CBV electrocatalyst solution was filtered using a vacuum pump filter system (0.45 μm nylon membrane) and washed vigorously with deionized water. The resulting catalyst material was vacuum-dried at 40 °C for 24 h. Then, the product was recovered and grounded by hand using a quartz mortar to obtain the final powder material.

2.4. Physical Characterization. First, the crystalline structure of the electrocatalysts was determined by powder X-ray diffraction (XRD) with a Rigaku SmartLab X-Ray diffractometer assembled with a Cu K_α radiation (λ = 1.54 Å) source. The 2θ range was scanned

https://doi.org/10.1021/acsaem.2c02843
ACS Appl. Energy Mater. 2022, 5, 15175−15187

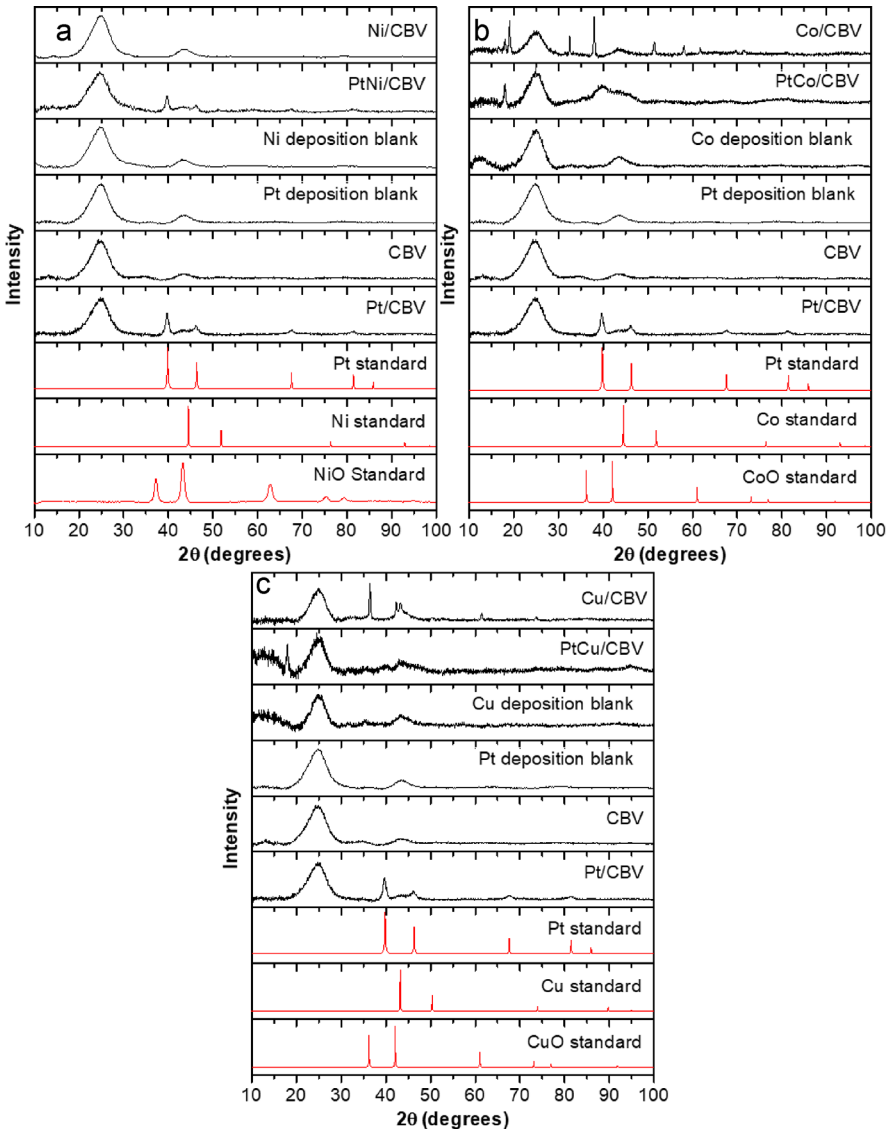

Figure 2. PXRD patterns for (a) Ni catalysts, (b) Co catalysts, and (c) Cu catalysts with their corresponding commercial standards.

between 10 and 100° at a rate of 0.02° s^{-1}. Smart lab software was used to acquire the data and for background correction. Origin software was used for further peak processing and smoothness of the signals using the Savitzky−Golay filter. The structural morphology of the as-prepared samples was confirmed using HR-TEM images taken with a 200 kV JEOL JEM 2100F instrument in the Center for Functional Nanomaterials (CFN) at the Brookhaven National Laboratory (BNL) and a 200 kV JEOL ARM 2200 in the Instituto de Investigación de Materiales of the Universidad Nacional Autónoma de México. The latter instrument is a spherical aberration-corrected scanning transmission electron microscope (Cs-STEM) operated in the STEM mode at an accelerating voltage of 80 or 200 kV coupled with an energy-dispersive X-ray spectrometer (EDS). Micrographs were recorded and analyzed with a Gatan Microscopy Suite (Digital Micrograph), and the X-ray microanalysis was processed with a TEM EDS Analysis System (EDAX). The metal concentration was determined using an Optima 8000 PerkinElmer inductively coupled plasma (ICP)−optical emission spectroscopy (OES) with standard plasma parameters, as shown in Table S1. For the ICP-OES analyses, the metal catalysts were dissolved following a digestion procedure. Six samples of ca. 3 mg were digested with 10 mL of aqua regia and heated to simmering until ca. 0.5 mL remained. After cooling down to room temperature, the dissolved metals were reconstituted with 2% HNO_3 solution using a quartz filter.

2.5. Electrochemical Characterization. Cyclic voltammetry (CV) was used to characterize the electrocatalysts after the RoDSE and SGD methodology. A typical electrochemical setup consisting of a three-electrode assembly was used. The setup was composed of a GC WE that was cleaned before every experiment by polishing the GC surface with alumina micro-polish (Buehler) (1.0, 0.5, and 0.03 μm) and pure water in an eight-shape pattern, a Ag/AgCl sat. KCl (CH Instruments Inc.) or a mercury oxide (HgO/Hg) (CH Instruments Inc.) reference electrode, and a platinum wire counter electrode (CE) along with a Biologic V30 potentiostat and RDE setup.[37]

For the electrochemical cleaning, the GC electrode was cycled at a potential window between −1.0 and 1.6 V vs RHE at potential scan rates of 100, 50, and 20 mV/s in 0.1 M KOH. Then, an ink dispersion of an 8:2:0.2 volume ratio of pure water, isopropanol (Sigma-Aldrich), and Nafion (10% solution in alcohol, Sigma-Aldrich), respectively, with the electrocatalyst was sonicated for a minimum of 30 min. A 10 μL aliquot was drop-casted on the GC electrode and dried using an IR lamp and left at ambient temperature. Finally, a CV was obtained at the Pt potential window from 0.1 to 1.2 V versus the RHE at a scan rate of 25 mV/s in an argon saturated 0.1 M KOH aqueous solution.

2.6. Rotating Disk Electrode ORR Experiments. The RDE linear sweep voltammetry (LSV) measurements were done to lower the capacitive currents, starting at 1.2 V and finishing at 0.0 V versus

https://doi.org/10.1021/acsaem.2c02843
ACS Appl. Energy Mater. 2022, 5, 15175−15187

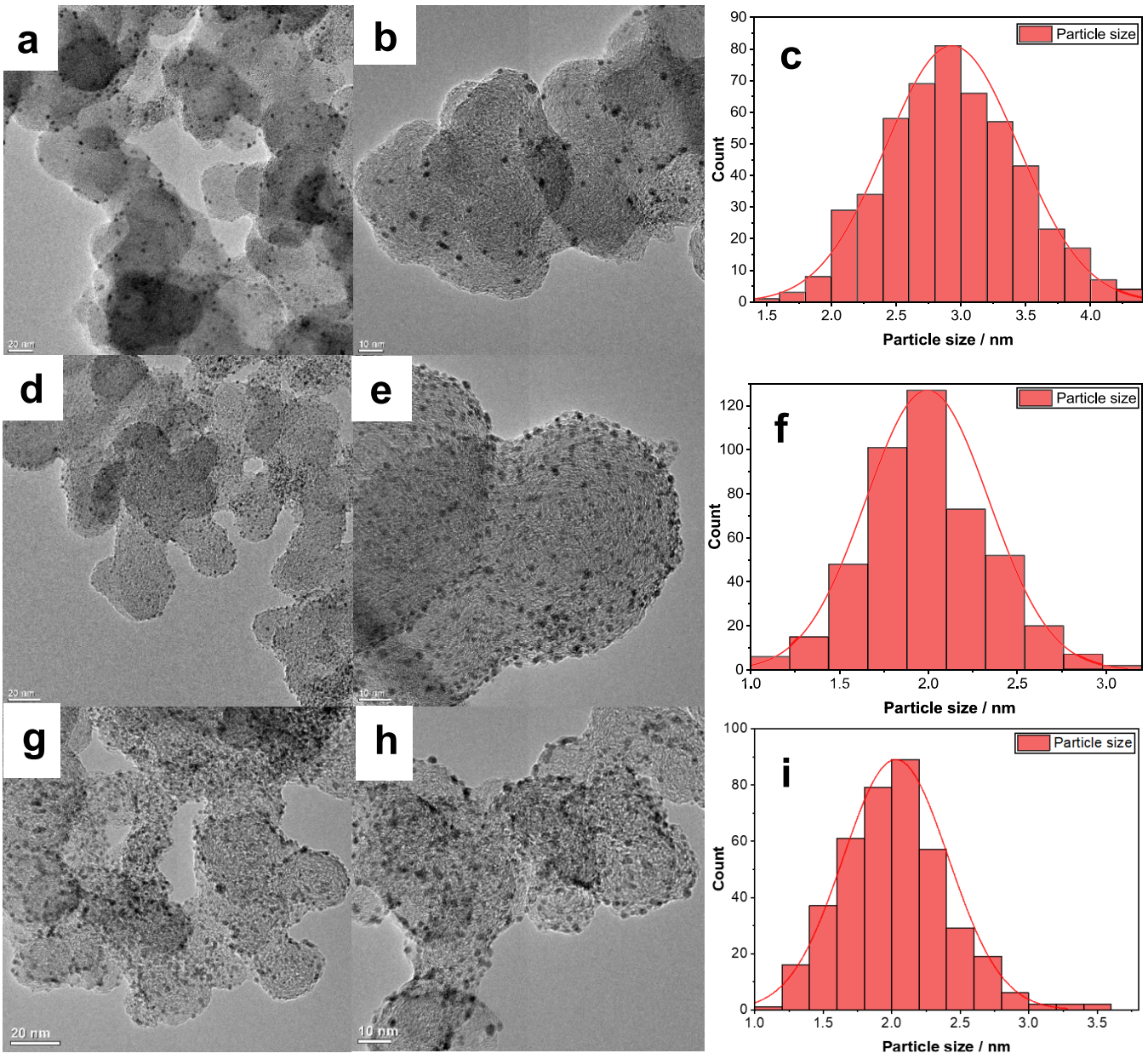

Figure 3. Transmission electron microscopy images of PtM/CBV electrocatalysts and their respective particle size distributions: (a–c) PtNi/CBV, (d–f) PtCo/CBV, and (g–i) PtCu/CBV.

the RHE at a scan rate of 10 mV/s and 1600 rpm in an argon saturated 0.1 M KOH aqueous solution. An additional LSV was acquired at the same potential window, scan rate, and revolutions per minute while under O_2 saturated 0.1 M KOH solution. The Koutecky–Levich (KL) plots were done with LSV data taken at 400, 625, 900, 1225, 1600, and 2025 rpm. The ORR polarization curves were used to calculate the number of electrons, n, transferred by using the KL and Levich eqs 1 and 2, respectively.

$$\frac{1}{j_L} = \frac{1}{j_k} + \frac{1}{\sqrt{B\omega}} \quad (1)$$

Here, j_L is the limiting diffusional current density, j_k is the activation controlled current density, ω is the rotation rate of the RDE, and B represents $0.62nF\,C(O_2)\,D_0^{2/3}\nu^{-1/6}$, which is also the Levich equation slope seen in eq 2.

$$j_L = 0.62nF\,D_0^{2/3}\nu_0^{-1/6}\,C_0\omega^{1/2} \quad (2)$$

Here, n is the number of transferred electrons through the reaction, F is the Faraday's constant (96,487 C/mol), D_0 is the oxygen diffusion coefficient, ν_0 is the kinematic viscosity, C_0 is the gas solubility (i.e., O_2) in the electrolyte, and w is the rotating rate in revolutions per minute. In 0.1 M KOH solution, D_0, ν_0, and C_0 were 1.9×10^{-5} cm^2/s, 8.7×10^{-3} cm^2/s, and 1.22×10^{-6} mol/cm^3, respectively.

Accelerated durability experiments were done to test the stability of the electrocatalysts after 30,000 CV cycles under ORR conditions. The procedure was as follows: (1) A CV was obtained under an argon environment using the Pt potential window at a scan rate of 25 mV/s. (2) Under both Ar and O_2 saturated 0.1 M KOH aqueous solution, LSVs were recorded as described in the RDE section. (3) Ten thousand CV cycles between 0.6 and 0.95 V versus the RHE were recorded at a scan rate of 100 mV/s. (4) Steps 1, 2, and 3 were repeated two more times.

For the OER experiments, LSV was done starting at 1.1 V and ending at 1.7 V versus the RHE in O_2 saturated 0.1 M KOH solution at 10 mV/s and 1600 rpm. The overpotential was calculated considering the OER redox potential (1.23 V vs SHE) and the

https://doi.org/10.1021/acsaem.2c02843
ACS Appl. Energy Mater. 2022, 5, 15175−15187

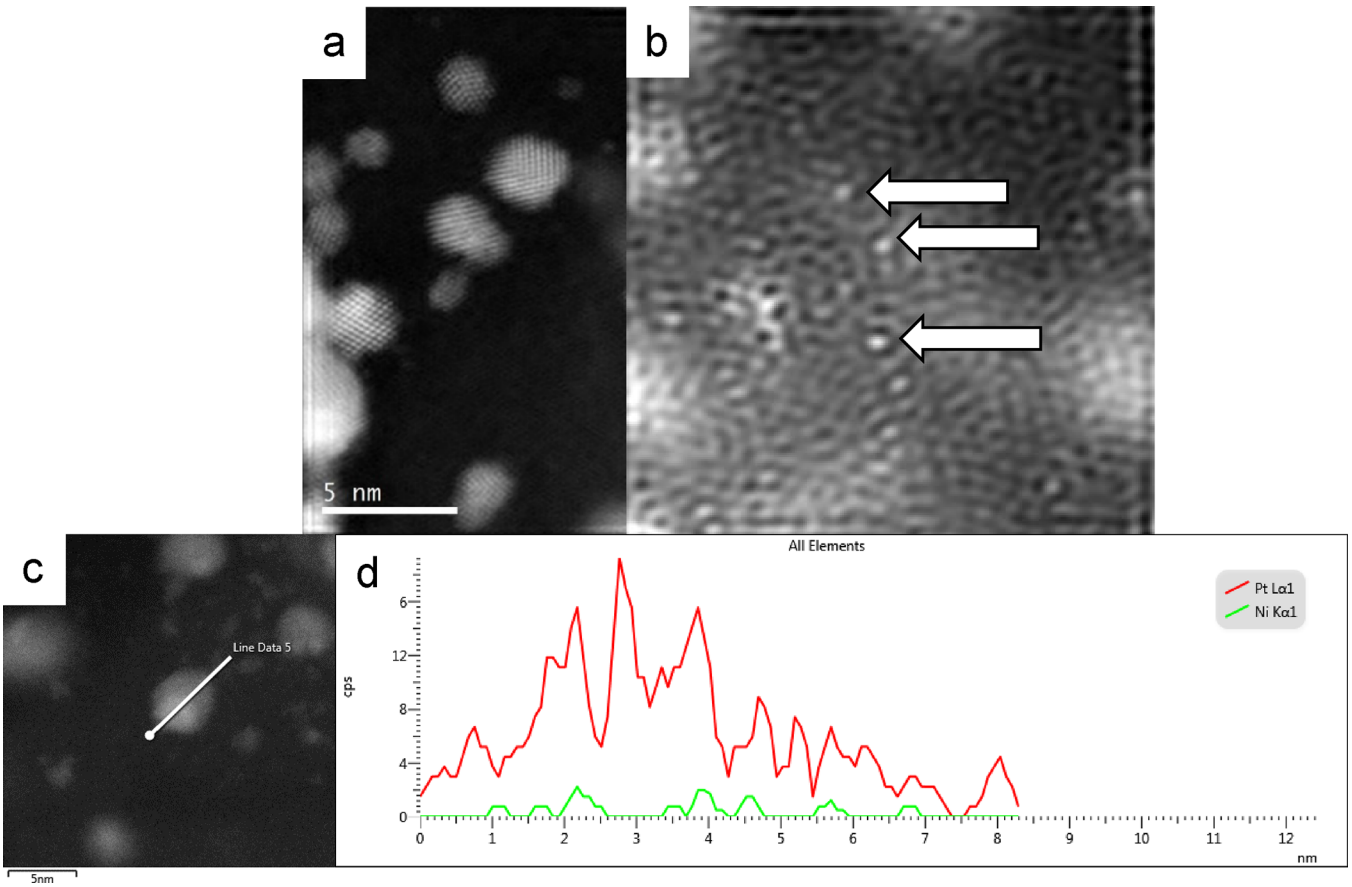

Figure 4. High-resolution scanning transmission electron microscopy images of (a) Pt clusters with different shapes, (b) single atoms of Pt indicated by arrows, and (c) PtNi/CBV for the (d) X-ray fluorescence−energy dispersive spectroscopy line scan profile.

potential obtained at a current density of 10 mA/cm^2, considering the geometric area of our GC RDE electrode (0.1963 cm^2). The Pt/CBV 20% commercial catalyst used in all the experiments was purchased from the Fuel Cell Store.

2.7. Ex Situ X-ray Absorption Spectroscopy Electrochemical Experiments. X-ray absorption spectroscopy (XAS), X-ray absorption near edge structure (XANES),[38] and extended X-ray absorption fine structure (EXAFS),[39] experiments were done at 7-BM QAS at the Brookhaven National Laboratory NSLS-II beamline. The Pt L_3 absorption energy edge data were collected in the fluorescence mode using a PIPS detector. Further data processing—calibration, normalization, fittings—was done using the IFEFFIT package (ATHENA and ARTEMIS).[40]

2.8. In Situ X-ray Absorption Spectroscopy Electrochemical Experiments. The PtCo/CBV and the commercial Pt/CBV electrocatalysts were tested for in situ XAS electrochemical experiments. The same beamline described in the ex situ XAS[41] procedure and data processing was used. A three-electrode in situ electrochemical cell was used, and the same procedure described in our previous publication was followed.[42]

3. RESULTS AND DISCUSSION

3.1. RoDSE Synthesis Parameters. The electrocatalyst reduction potential was found using homogeneous electrochemical experiments. It is worth mentioning that the electrolyte plays a crucial role in electrodeposition experiments. This is mainly related to the pH, anion, and electrochemical potential relationships. These relationships suggest that different electroactive species are more stable under applied electrochemical potentials at different pH conditions. For example, the reduction of Ni at the pH range of 0−14 occurs between ca. −0.5 and −3.0 V versus the SHE.[43,44] At low potentials, there is competition with the HER. On the other hand, it has been found that nickel precipitates at pH values higher than 6.8 and pH 4 is an optimal value for electrodeposition.[45] Considering these constraints, the nickel precursor was dissolved in 0.1 M $KClO_4$ and a CV at 10 mV/s was run in the potential range between −1.0 and 1.7 V to find a reduction process associated with Ni (see Figure S1a). In this CV, oxygen evolution is seen at ca. 1.4 V. When reversing the potential scan, a reduction process starts at ca. −0.75 V, ultimately resulting in a significant current associated with the HER, which could also be related to the reduction of Ni.[46] Similarly, the same experimental procedure to find the Co and Cu reduction potentials was employed. As shown in Figure S1b,c, the electrodeposition potentials were −0.75 and −0.80 V for Co and Cu, respectively. These reduction potentials were used to electrodeposit M on the CBV support with the RoDSE methodology, as seen in Figure S2. Then, using SGD, the final electrocatalysts consisting of PtM/CBV were obtained due to the difference in standard reduction potentials between Pt and Ni, Co, or Cu.

3.2. Powder X-ray Diffraction. The crystalline structure of the electrocatalysts was confirmed with PXRD (see Figure 2). First, the measurements were done for the Ni/CBV, Co/CBV, and Cu/CBV. For Ni/CBV, see Figure 2a; no peaks were associated with Ni diffraction, although two peaks can be seen at ca. 25 and 43° associated with the CBV diffraction. When modifying the Ni/CBV with Pt by SGD, the PtNi/CBV

https://doi.org/10.1021/acsaem.2c02843
ACS Appl. Energy Mater. 2022, 5, 15175−15187

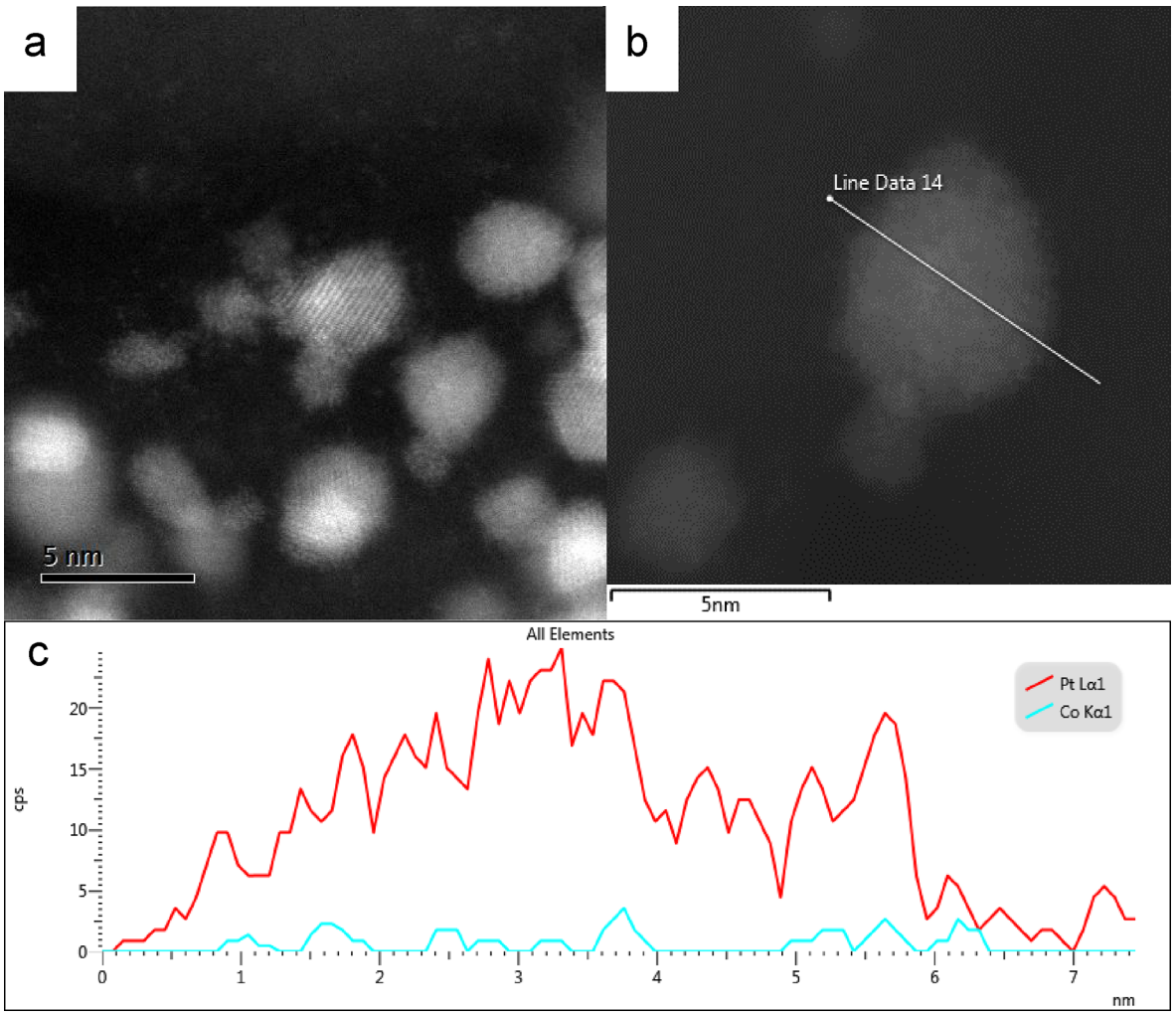

Figure 5. High-resolution scanning transmission electron microscopy images of (a) Pt clusters with different shapes and (b) STEM image of the PtCo/CBV for the (c) EDS line scan profile.

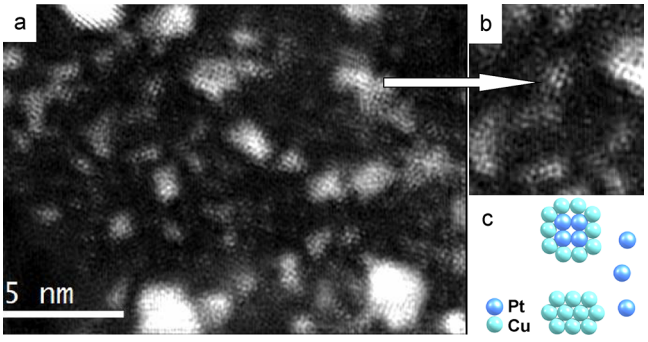

Figure 6. High-resolution scanning transmission electron microscopy images of (a) PtCu/CBV sample clusters with different shapes and (b) Pt clusters surrounded by Cu atoms and (c) a diagram representation of Pt cluster surrounded by Cu atoms, Cu clusters, and Pt single atoms.

diffractogram shows peaks associated with Pt diffraction at 39.9° (111), 46.5° (200), and 67.9° (220) attributed to fcc Pt.[47] To corroborate further if the PtNi/CBV material product is obtained by the presence of electrochemically reduced Ni/CBV and not just an absorption process of the materials in solution, a RoDSE blank experiment was done following the RoDSE methodology at an open-circuit potential (without applying a reduction potential). The materials were recovered and cataloged as the sample's respective blanks (e.g., Ni blank and PtNi blank). The Ni deposition blank shows a similar diffractogram to the Ni/CBV sample. However, the PtNi/CBV blank (obtained by simulating an SGD using the Ni deposition blank sample and the Pt precursor) does not show any Pt diffraction peak. These simulated experiment results conclude that Pt's presence in the PtNi/CBV sample is attributed to Pt's SGD of Ni/CBV obtained by RoDSE. A similar analysis was done for the Co/CBV and Cu/CBV samples. However, in these cases, for both samples, some diffraction peaks were associated with a mixture of reduced Co and CoO (for the Co/CBV) and reduced Cu and CuO (for the Cu/CBV); see Figure 2b,c. Similar peak positioning of Pt diffraction in the PtNi/CBV can be seen for PtCo/CBV and PtCu/CBV samples.

3.3. Transmission Electron Microscopy and Inductively Coupled Plasma. To further corroborate the shape and particle size distribution of the PtM/CBV prepared by RoDSE-SGD, TEM and HRTEM were done. As shown in Figure 3, the TEM of the PtM/CBV nanoparticles are well dispersed with narrow size distributions. The resulting average particle sizes were 3, 2, and 2 nm for PtNi/CBV, PtCo/CBV, and PtCu/CBV, respectively. To obtain the elemental composition of the nanoparticles, ICP-OES was used, and

https://doi.org/10.1021/acsaem.2c02843
ACS Appl. Energy Mater. 2022, 5, 15175−15187

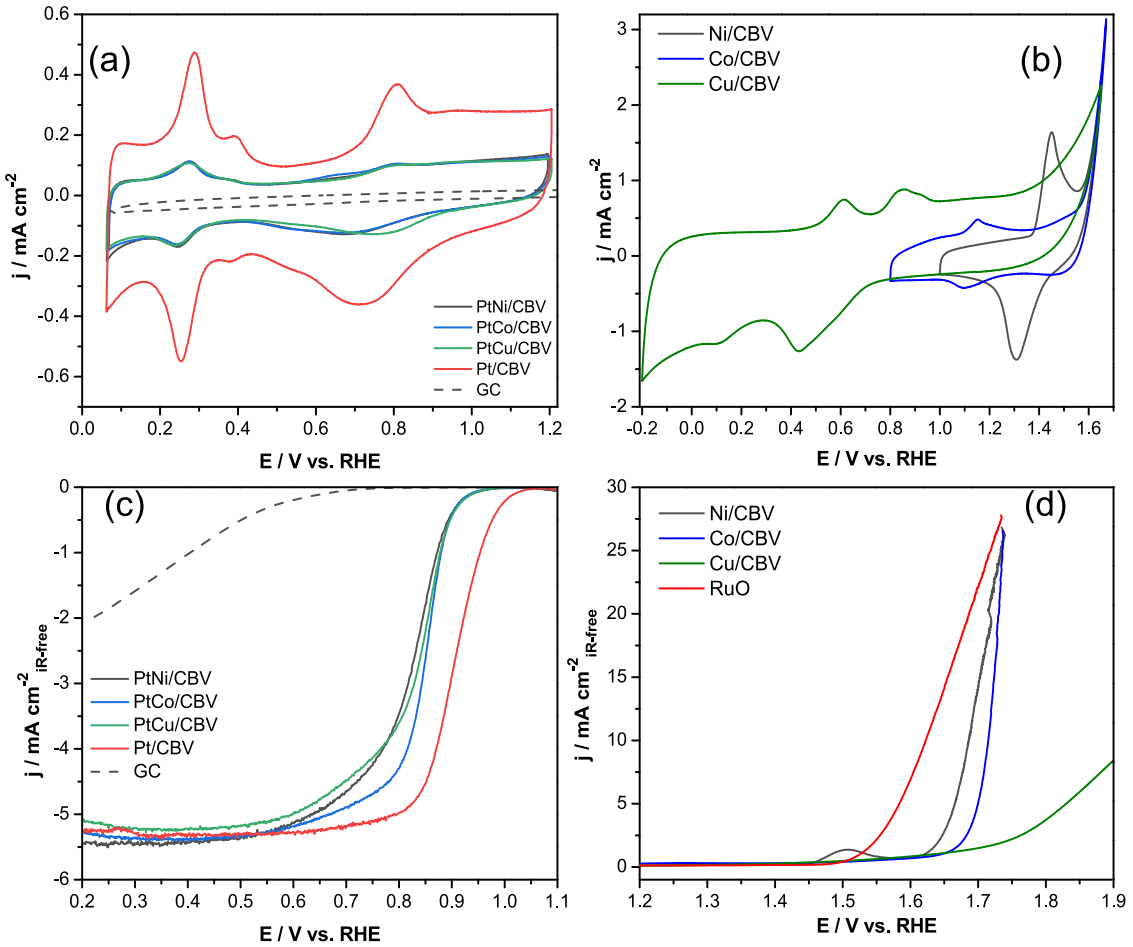

Figure 7. Cyclic voltammograms of (a) PtNi/CBV, PtCo/CBV, PtCu/CBV, and commercial Pt/CBV and (b) Ni/CBV, Co/CBV, and Cu/CBV at their respective potential windows at 25 mV/s. (c) ORR polarization curves of PtNi/CBV, PtCo/CBV, PtCu/CBV, and commercial Pt/CBV at 10 mV/s at 1600 rpm. (d) OER polarization curves of Ni/CBV, Co/CBV, Cu/CBV, and commercial RuO at 10 mV/s and 1600 rpm. All the experiments were done in 0.1 M KOH.

the results demonstrated that the PtNi/CBV, PtCo/CBV, and PtCu/CBV had a Pt % of 1.7 ± 0.2, 1.9 ± 0.3, and 3.0 ± 0.1, respectively (see Table S2).

Further analysis with high-angle annular dark-field scanning transmission electron microscopy (HAADF-STEM) was done on the PtM/CBV materials. PtNi/CBV typical HAADF images are shown in Figure 4a,b. In these images, the Pt is present in two forms. We can see in Figure 4a, Pt nanoparticles with four shapes, namely, decahedral, fcc, octahedral, and fcc single twinned. Their atomic spacing corresponds to Pt (110) and more prominent (111) planes. In addition, there are single Pt atoms as shown in Figure 4b. Those atoms seem to be interacting with the carbon substrate.

The line scan profile seen in Figure 4d shows the presence of both Pt and Ni and their respective EDS chemical analysis, shown in Figure S3, and indicates that there is Pt present on the nanoparticles. It is more likely that Ni atoms are occupying a substitutional site of the Pt. For the PtCo/CBV sample seen in Figure 5, we see similar features to the PtNi/CBV; the particles have the same characteristics. However, the sample with PtCu/CBV shows important differences. HAADF images shown in Figure 6a,b show large particles as well as small clusters and single atoms. The amplified region of the image (Figure 6b) shows small clusters, where the one indicated by the arrow is a cluster made of four Pt atoms forming a square surrounded by Cu atoms.

3.4. Oxygen Reduction Reaction Catalytic Activity.

The aim of obtaining a low Pt loading was achieved using the RoDSE methodology. However, the electrochemical activity of these electrocatalysts needed to be tested. The voltammogram shapes of the PtM/CBV, seen in Figure 7a, show the typical electrochemical processes associated with a Pt electrode voltammogram in 0.1 M KOH. The difference comes in the current values of the voltammograms when compared with the lab-made materials (that had lower currents) and the commercial Pt/CBV 20% catalyst. This variance is mainly related to their difference in Pt %, proving again that our lab-made materials had low Pt loadings. Figure 7b also shows characteristic CV patterns for Ni, Co, and Cu redox processes.[48,49] It is also confirmed that Ni is present in the Ni/CBV catalysts obtained by RoDSE electrodeposition.[49]

The electrochemical performance of the PtM/CBV catalysts were tested for ORR, as seen in Figure 7c, using a mass loading of 100 $\mu g/cm^2_{geo}$. PtCo/CBV had a closer half-wave potential to that of the commercial catalysts with an $E_{1/2}$ of 0.85 V versus the RHE. The M/CBV precursors were further tested for the OER, and Ni/CBV, as seen in Figure 7d, showed a lower overpotential with 450 mV at 10 mA/cm^2_{geo}.

https://doi.org/10.1021/acsaem.2c02843
ACS Appl. Energy Mater. 2022, 5, 15175−15187

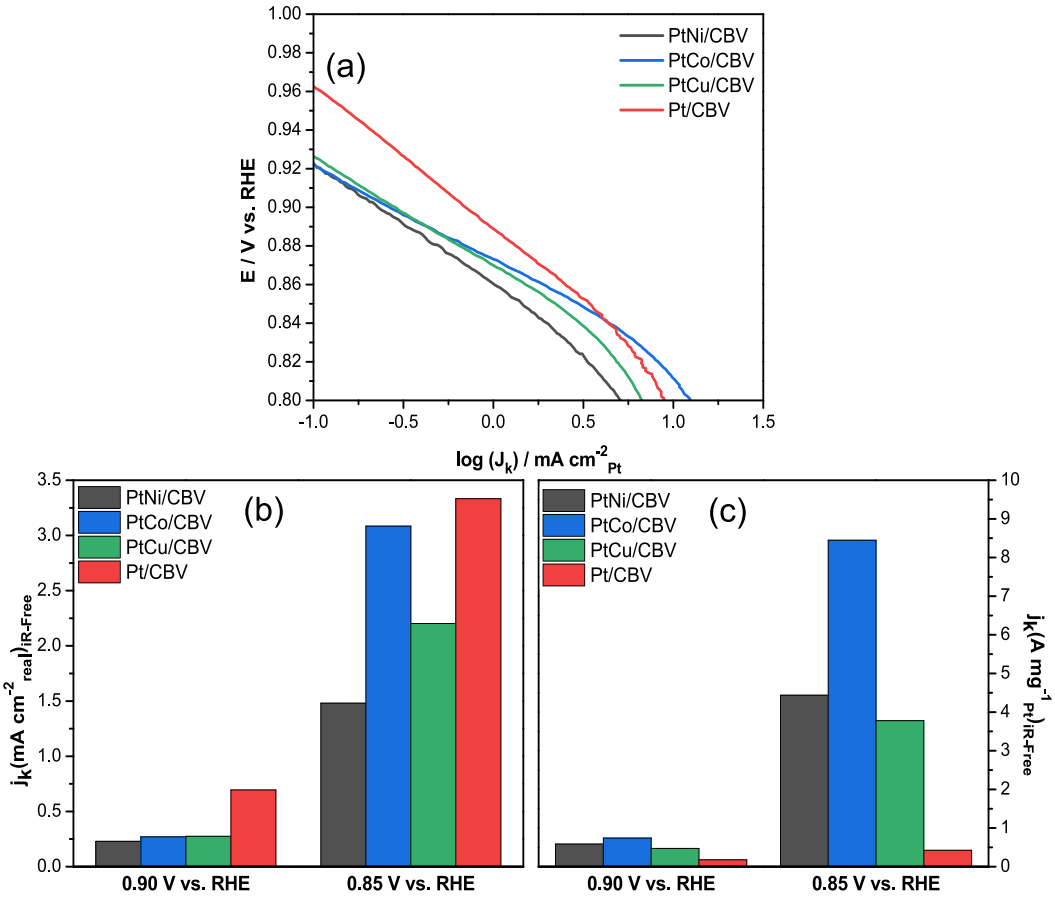

Figure 8. (a) Tafel plots, (b) specific activities, and (c) mass activities for the PtM/CBV catalysts derived from the kinetic current of the Tafel plots.

Table 1. Summary of All Catalyst Oxygen Reduction Properties in the Alkaline Medium Compared with State-of-the-Art Materials in KOH

				specific activity ($mA/cm^2_{Pt\ if\ not\ specified}$)		mass activity ($A/mg_{Pt\ if\ not\ specified}$)	
catalyst	mass loading ($\mu g/cm^2_{geo}$)	E_{onset}(V) vs RHE	$E_{1/2}$(V) vs RHE	0.90 V	0.85 V	0.90 V	0.85 V
PtNi/CBV	100_{total}	0.98	0.83	0.229	1.480	0.584	4.436
PtCo/CBV	100_{total}	1.00	0.85	0.271	3.083	0.741	8.446
PtCu/CBV	100_{total}	1.02	0.84	0.275	2.202	0.472	3.777
Pt/CBV 20%	100_{total}	1.04	0.90	0.694	3.332	0.177	0.424
PdCu/C[55]	25_{Pd}		0.89	2.30_{Pd}		0.130_{Pd}	
Pt_3Co/C[56]	367_{total}		0.93			3.7	
Pt/C(TKK)[56]	367_{total}		0.88			0.19	

To determine the ORR number of electrons transferred for each electrocatalyst, KL analysis was done using eqs 1 and 2. The KL plots seen in Figure S5 were obtained and used to get the Levich slope and solve the equations for n. The provided n values were 4, 3.9, and 4 for PtNi/CBV, PtCo/CBV, and PtCu/CBV, respectively. This indicates that all the electrocatalysts reduced molecular oxygen to OH^- through the four-electron pathway. Tafel analysis, seen in Figure 8a, was done to understand the kinetics of the ORR after the calculation of the kinetic current densities (j_k)[50] at a fixed rotation rate speed (1600 rpm) using eq 3:

$$j_k = \frac{j}{1 - \left(\frac{j}{j_L}\right)} \tag{3}$$

Different Tafel slopes could be obtained depending on the electrocatalyst and electrolytes that are chosen.[51] For the Pt catalyst under acidic conditions, two Tafel slopes are typically obtained with values of 60 mV/decade in the high-overpotential region (HOPR), which is beyond 0.8 V versus the RHE, and 120 mV/decade in the low-overpotential region (LOPR), which is below 0.8 V versus the RHE.[52] In the alkaline medium, specifically 0.1 M KOH, slope values for Pt

https://doi.org/10.1021/acsaem.2c02843
ACS Appl. Energy Mater. 2022, 5, 15175−15187

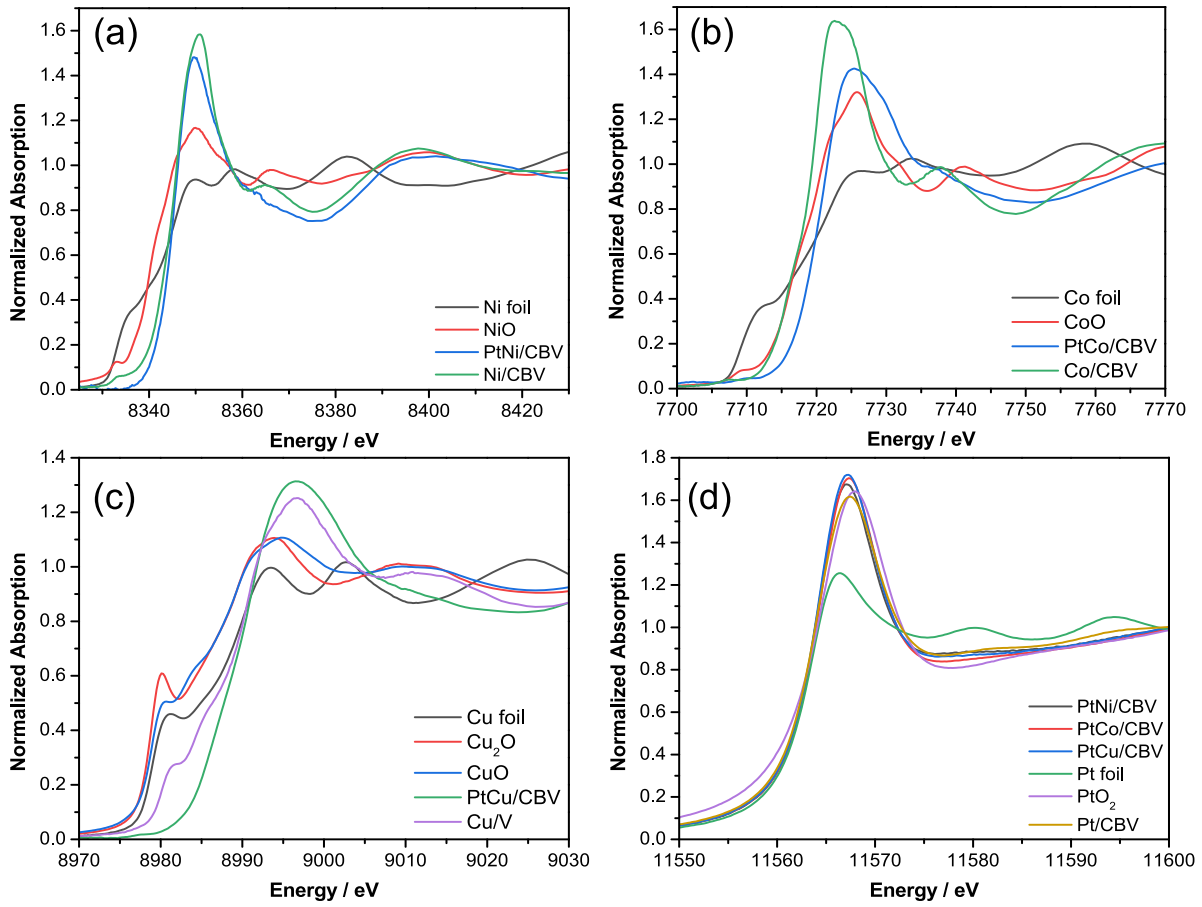

Figure 9. Ex situ XANES spectra for (a) Ni K-edge, (b) Co K-edge, (c) Cu K-edge, and (d) Pt L_3-edge for the respective PtM/CBVs with their respective standards.

are typically equal to 60 mV/decade in the HOPR and 200–490 mV/decade in the LOPR.[53,54] In addition, Pt alloys in an alkaline medium could have values as low as 47 mV/decade in the HOPR to as high as 304 mV/decade in the LOPR.[51] Our electrocatalysts comply with these values, suggesting similar Pt catalyst kinetics in the alkaline medium, obtaining values for PtNi/CBV, PtCo/CBV, PtCu/CBV, and Pt/CBV 20% in the HOPR of 68, 54, 65, and 79 mV/decade and, in the LOPR, 197, 253, 238, and 229 mV/decade, respectively.

The Tafel analysis was further used to determine the specific and mass activities. The specific activities (mA/cm^2_{real}), seen in Figure 8b, of our catalysts were close to each other with values of 0.229, 0.271, and 0.275 mA/cm^2_{real} at 0.90 V and 1.480, 3.083, and 2.202 mA/cm^2_{real} values at 0.85 V for PtNi/CBV, PtCo/CBV, and PtCu/CBV, respectively. However, the Pt/CBV commercial catalysts had 0.694 mA/cm^2_{real} at 0.90 V and 3.332 mA/cm^2_{real} at 0.85 V. These were expected results, considering that the commercial catalyst had a lower overpotential in the ORR polarization curves. The determinant difference, their performance, was analyzed by mass activities (A/mg^1_{Pt}) (seen in Figure 8c), an important parameter for catalyst efficiency in terms of cost. All the RoDSE-SGD lab-made electrocatalysts surpassed the Pt/CBV 20% commercial catalyst with PtCo/CBV having the highest values with 0.741 A/mg at 0.90 V and 8.446 A/mg at 0.85 V. See Table 1 for a summary of our RoDSE-SGD ORR catalysts results compared with reported PGM materials and commercial Pt/C catalysts.

3.5. ORR Catalyst Durability Experiments. Considering that PtCo/CBV and PtNi/CBV gave higher mass activities values, their ORR performance was examined with accelerated durability experiment tests in 0.1 M KOH, as seen in Figure S6. Both catalysts exhibited good performance through 10,000 CV potential ORR cycles. PtNi/CBV gave the best overpotential resulting in 5 mV compared to PtCo/V and commercial Pt/CBV with 28 and 27 mV, respectively. After 30,000 cycles, the catalysts remained active, and comparable overpotential results to Pt/CBV were obtained for PtNi/CBV and PtCo/CBV with 40 and 50 mV, respectively. Although our most active catalyst—considering the PGM mass—did not retain higher $E_{1/2}$ activity after 30,000 cycles, their overpotential performance was similar to that of the Pt/CBV commercial catalyst, suggesting that they are suited for further AEMFC studies.

3.6. Ex Situ X-ray Absorption Spectroscopy. All the catalysts samples were characterized by ex situ XAS, as seen in Figure 9. Depending on the selected energy, a specific electronic transition will be obtained, serving as a probe to identify our elemental species. The study focused on the XANES region to obtain information regarding the samples' electronic structure and the local chemical environment. The obtained XANES spectra were compared with their respective metal and metal oxide standards. However, it is important to highlight that first-row transition metals using the K-edge can exhibit what is called the forbidden transition (1s → 3d), which is associated with a pre-edge absorption peak. The Ni samples Ni/CBV and PtNi/CBV, shown in Figure 9a, exhibit higher intensities than those of the NiO and Ni foil standards, suggesting that the samples are both oxidized. However, the

https://doi.org/10.1021/acsaem.2c02843
ACS Appl. Energy Mater. 2022, 5, 15175−15187

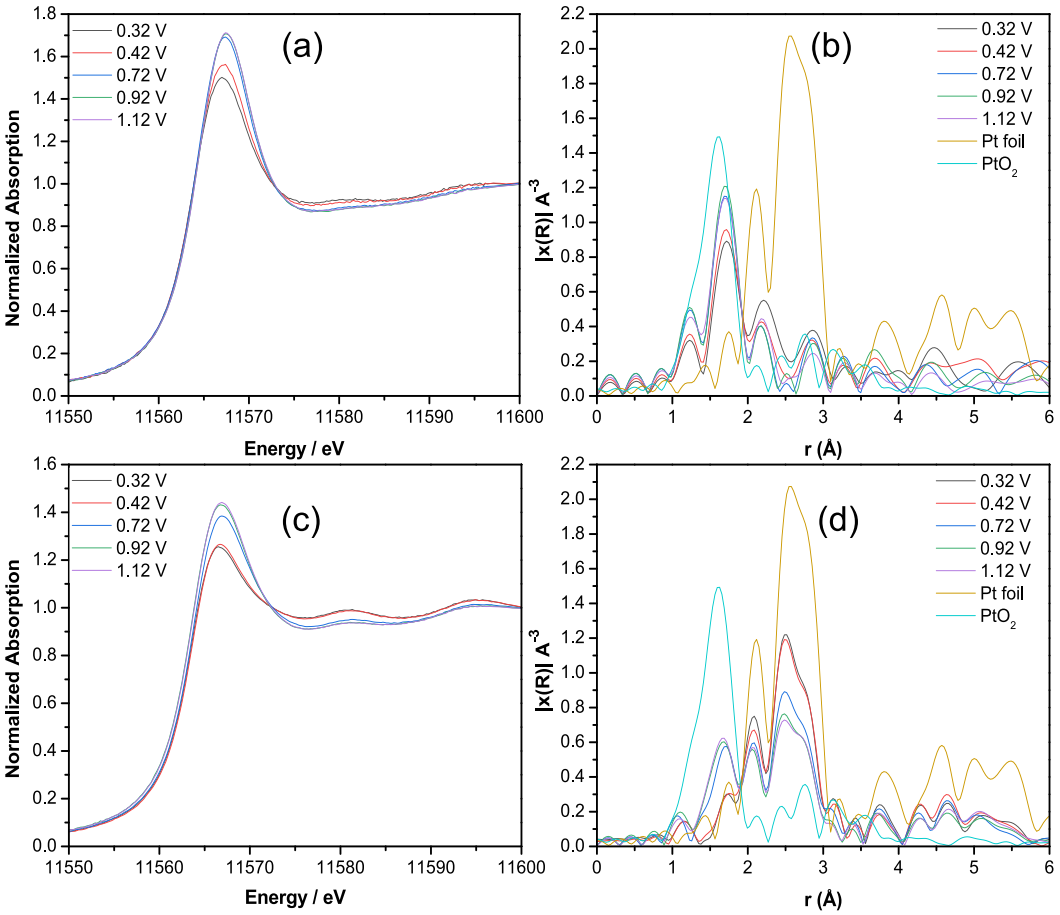

Figure 10. In situ electrochemical experiments in air saturated 0.1 M KOH using the Pt L_3-edge for the (a, c) XANES region and (b, d) EXAFS radial analysis of PtCo/CBV and Pt/CBV 20% commercial catalysts, respectively. The applied potentials were 0.32, 0.42, 0.72, 0.92, and 1.12 V vs the RHE.

intensity of Ni/CBV was higher than that of PtNi/CBV. This could indicate that Pt is donating electrons to Ni or, since Ni is expected to be in the core of the PtNi/CBV sample, Ni is not being oxidized by air, resulting in a more reduced Ni species. The Co sample shows a similar behavior as seen in Figure 9b. Both Co/CBV and PtCo/CBV have higher absorption edge intensities than the standards. A lower intensity is observed in PtCo/CBV compared to Co/CBV, suggesting the same statement for the Ni sample. On the other hand, the Cu sample was different. Figure 9c shows that Cu in the Cu/CBV has a lower intensity, meaning that it is less oxidized compared to the Cu in the PtCu/CBV sample. This means that Cu is donating electrons to Pt. These Pt samples were then compared using the Pt L_3-edge, as seen in Figure 9d. The lab-made Pt samples show a similar spectrum with their intensity close by to the PtO_2 and Pt/CBV standards. This tells us that the Pt samples have more presence of oxide species.

3.7. In Situ X-ray Absorption Spectroscopy. Recognizing that PtCo/CBV gave the best ORR performance, this catalyst was studied via in situ electrochemical XAS experiments using the Pt L_3 absorption edge, as seen in Figure 10. These studies were done while air was permitted inside the electrochemical cell, simulating an ORR experiment. There is a clear relationship between the intensity of the Pt L_3 absorption edge white-line peak and the applied electrochemical potential in the XANES region for the PtCo/CBV and Pt/CBV 20% (see Figure 10a,b). As the applied potential turned more negative, a decrease in the white-line intensity was observed, indicating that the Pt species were reduced in both samples.

These experiments can further be related to classic ORR polarization curves obtained by RDE. First, the intensities of both samples at potentials 1.12 and 0.92 V are very similar. These potentials are associated with the onset potential region of the ORR. Then, it was noticed at 0.72 V that the intensity decreased more, suggesting that the ORR is happening. However, a more significant jump to lower intensities is seen in both samples between potentials 0.72 and 0.42 V. This is expected since this is a potential active region where the ORR occurs. Then, the white-line intensity at 0.32 V is very similar to 0.42 V, indicating that this may be the limiting current region for ORR. In addition, the white-line intensity of PtCo/CBV at 0.42 V is higher than that of Pt/C at 0.42 V, which is caused by the electronic/geometrical effects from Co or CoOx. This suggests that the d-band center of Pt on Co is lowered, which can be a cause of high ORR activity. This information clarifies that our catalyst undergoes an ORR on the Pt species and behaves similarly to a commercial catalyst with a much lower Pt content.

The EXAFS region was analyzed for radial distributions as shown in Figure 10b,d. Comparing the samples with Pt foil and PtO_2 standards, the PtCo/CBV sample showed at each potential a significant peak in the region of the Pt−O distance at ca. 1.6 Å (see Figure 10b). When the intensity of the Pt−Pt bond in the region of ca. 2.6 Å is analyzed, no clear difference

https://doi.org/10.1021/acsaem.2c02843
ACS Appl. Energy Mater. 2022, 5, 15175−15187

against the background noise for most of the potentials is observed. This suggests that the sample is a Pt oxide as it has a similar spectrum to the PtO_2 standard. Interestingly, at 0.42 and 0.32 V versus the RHE, the Pt−Pt bond peak had higher intensity while Pt−O reduced its intensity, suggesting that the Pt is changing from being PtO_2 to Pt^0. It could also be that the particles are very small, that is, single atom and cluster, as seen by HRSTEM, to exhibit the bouncing near-neighbor phenomenon of metal absorbers. On the other hand, the Pt/CBV 20% at each applied potential shows a similar spectrum to that of the Pt foil standard, suggesting that the sample is metallic. There is a clear peak at the Pt−Pt bond radial region, and a lower-intensity peak is located at the Pt−O bond region.

4. CONCLUSIONS

The RoDSE methodology was successfully explored for the first time to synthesize Ni, Co, and Cu nanoparticles supported on CBV. These nanoparticles were highly dispersed and had homogeneous diameter sizes of ca. 2−3 nm and proved to be active for the OER in alkaline medium. Combining the RoDSE methodology with SGD provided a simple and reliable method to obtain low-platinum content-modified Ni/CBV, Co/CBV, and Cu/CBV ORR catalyst materials. HRSTEM provided evidence of Pt single atoms in the PtNi/CBV and PtCo/CBV samples. On the other hand, Pt clusters and Cu clusters were observed for the PtCu/CBV samples. These PtM/CBV samples were submitted to multiple physical characterizations, and their electrochemical performance was examined for the ORR, which followed a four-electron pathway. Compared with all samples, the PtCo/CBV had the highest mass activity values of 0.741 and 8.446 A/mg_{Pt} at 0.90 and 0.85 V versus the RHE, respectively. For ORR durability experiments, PtNi/CBV and PtCo/CBV showed similar performance to that of commercial Pt/V 20% catalysts after 30,000 ORR voltammetric cycles of accelerated durability tests, suggesting that our catalysts can be further tested in AEMFCs. The samples' electronic structure was studied with XAS techniques, confirming the presence of all the elements in our samples, and the ex situ XAS studies suggested that all the samples were oxidized. Figure 10b suggests a very low Pt−Pt coordination number, which can be due to Pt single atoms (that have no Pt neighbors), as seen in the HRSTEM results.

The best ORR catalyst, PtCo/CBV, was further tested for in situ electrochemical XAS experiments. After monitoring the XANES region as a function of the potential, we concluded that this oxidized sample followed a typical ORR RDE experiment, having its white-line intensity decreased, which is thus associated with a less oxidized electronic structure as more negative potentials were applied. The EXAFS region also confirmed the oxide form of Pt (PtO_2) in the PtCo/CBV samples. The low Pt amount of the samples did not limit their ORR performance, suggesting that low percentages of PGMs should be incorporated into non-PGM catalysts to optimize mass activity performance directly related to catalyst costs and efficiency. These samples showed nanoparticles in the 2 nm diameter range, like quantum dots, and are close to single-atom and cluster catalysts. Ni/CBV, Co/CBV, and Cu/CBV materials were evaluated for their OER activity as well in which Ni/CBV had the lowest overpotential with 450 mV at 10 mA/cm^2_{geo} among the RoDSE-made catalysts.

■ ASSOCIATED CONTENT

Supporting Information

The Supporting Information is available free of charge at https://pubs.acs.org/doi/10.1021/acsaem.2c02843.

ICP-OES measurement parameters, cyclic voltammogram experiments to determine the reduction potentials for Ni, Co, and Cu, RoDSE chronoamperometries for Ni/CBV, Co/CBV, and Cu/CBV electrosynthesis, EDS results from HRSTEM studies, and RDE of ORR experiments (PDF)

■ AUTHOR INFORMATION

Corresponding Author

Carlos R. Cabrera − *Department of Chemistry and Biochemistry, University of Texas at El Paso, El Paso, Texas 79968, United States;* orcid.org/0000-0002-3342-8666; Email: crcabrerama@utep.edu

Authors

Joesene J. Soto Pérez − *Department of Chemistry, University of Puerto Rico, San Juan 00925-2537, Puerto Rico; Department of Chemistry and Chemical Biology, Cornell University, Ithaca, New York 14853, United States*

Armando Peña-Duarte − *Department of Chemistry and Biochemistry, University of Texas at El Paso, El Paso, Texas 79968, United States;* orcid.org/0000-0002-4286-5278

Pedro Trinidad − *Department of Chemistry, University of Puerto Rico, San Juan 00925-2537, Puerto Rico*

Gerardo Quintana − *Department of Chemistry, University of Puerto Rico, San Juan 00925-2537, Puerto Rico*

Xueru Zhao − *Chemistry Division, Brookhaven National Laboratory, Upton, New York 11973, United States*

Kotaro Sasaki − *Chemistry Division, Brookhaven National Laboratory, Upton, New York 11973, United States;* orcid.org/0000-0003-2474-8323

Miguel José Yacamán − *Department of Applied Physics and Materials Science, Northern Arizona University, Flagstaff, Arizona 86011, United States*

Rubén Mendoza-Cruz − *Instituto de Investigaciones en Materiales, Universidad Nacional Autónoma de México, México 04510, Mexico;* orcid.org/0000-0002-8831-1983

Complete contact information is available at: https://pubs.acs.org/10.1021/acsaem.2c02843

Notes

The authors declare no competing financial interest.

■ ACKNOWLEDGMENTS

This work was supported by the National Science Foundation NSF-PREM: Center for Interfacial Electrochemistry of Energy Materials (CiE^2M) grant no. DMR-1827622. This research used resources of the 7-BM QAS beamline of the National Synchrotron Light Source II, a U.S. Department of Energy (DOE) Office of Science User Facility, operated for the DOE Office of Science by Brookhaven National Laboratory (BNL) under contract no. DE-SC0012704. We appreciate the discussions with Miomir Vukmirovic (BNL) and thank the Instituto de Investigación de Materiales Universidad Nacional Autónoma de México (UNAM) for the use of the TEM core. C.R.C. acknowledges the STARs Award (2021) of the University of Texas System. J.J.S.P. acknowledges the Cornell Energy Systems Institute (CESI) and the Kavli Institute at

Cornell (KIC). The paper is partially adapted from J.J.S.P.'s PhD thesis (University of Puerto Rico at Río Piedras Campus 2022).

REFERENCES

(1) Dawood, F.; Anda, M.; Shafiullah, G. M. Hydrogen Production for Energy: An Overview. *Int. J. Hydrogen Energy* **2020**, *45*, 3847−3869.
(2) Department of Energy Home Page. *DOE Launches Bipartisan Infrastructure Law's $8 Billion Program for Clean Hydrogen Hubs Across U.S.*; https://www.energy.gov/articles/doe-launches-bipartisan-infrastructure-laws-8-billion-program-clean-hydrogen-hubs-across (accesed August, 2022).
(3) Beswick, R. R.; Oliveira, A. M.; Yan, Y. Does the Green Hydrogen Economy Have a Water Problem? *ACS Energy Lett.* **2021**, *6*, 3167−3169.
(4) Tellez-Cruz, M. M.; Escorihuela, J.; Solorza-Feria, O.; Compañ, V. Proton Exchange Membrane Fuel Cells (PEMFCs): Advances and Challenges. *Polymer* **2021**, *13*, 3064.
(5) Bai, J.; Ke, S.; Song, J.; Wang, K.; Sun, C.; Zhang, J.; Dou, M. Surface Engineering of Carbon-Supported Platinum as a Route to Electrocatalysts with Superior Durability and Activity for PEMFC Cathodes. *ACS Appl. Mater. Interfaces* **2022**, *14*, 5287−5297.
(6) Wang, Y.; Yang, Y.; Jia, S.; Wang, X.; Lyu, K.; Peng, Y.; Zheng, H.; Wei, X.; Ren, H.; Xiao, L.; Wang, J.; Muller, D. A.; Abruña, H. D.; Hwang, B. J.; Lu, J.; Zhuang, L. Synergistic Mn-Co Catalyst Outperforms Pt on High-Rate Oxygen Reduction for Alkaline Polymer Electrolyte Fuel Cells. *Nat. Commun.* **2019**, *10*, 1506.
(7) Liu, D.; Zeng, Q.; Hu, C.; Liu, H.; Chen, D.; Han, Y.; Xu, L.; Yang, J. Core−Shell CuPd@NiPd Nanoparticles: Coupling Lateral Strain with Electronic Interaction toward High-Efficiency Electrocatalysis. *ACS Catal.* **2022**, *12*, 9092−9100.
(8) Sasaki, K.; Kuttiyiel, K. A.; Adzic, R. R. Designing High Performance Pt Monolayer Core−Shell Electrocatalysts for Fuel Cells. *Curr. Opin. Electrochem.* **2020**, *21*, 368−375.
(9) Zeng, R.; Yang, Y.; Feng, X.; Li, H.; Gibbs, L. M.; DiSalvo, F. J.; Abruña, H. D. Nonprecious Transition Metal Nitrides as Efficient Oxygen Reduction Electrocatalysts for Alkaline Fuel Cells. *Sci. Adv.* **2022**, *8*, No. eabj1584.
(10) Toda, T.; Igarashi, H.; Uchida, H.; Watanabe, M. Enhancement of the Electroreduction of Oxygen on Pt Alloys with Fe, Ni, and Co. *J. Electrochem. Soc.* **1999**, *146*, 3750−3756.
(11) Xie, X.; Du, L.; Yan, L.; Park, S.; Qiu, Y.; Sokolowski, J.; Wang, W.; Shao, Y. Oxygen Evolution Reaction in Alkaline Environment: Material Challenges and Solutions. *Adv. Funct. Mater.* **2022**, *32*, 2110036.
(12) Bao, F.; Kemppainen, E.; Dorbandt, I.; Xi, F.; Bors, R.; Maticiuc, N.; Wenisch, R.; Bagacki, R.; Schary, C.; Michalczik, U.; Bogdanoff, P.; Lauermann, I.; van de Krol, R.; Schlatmann, R.; Calnan, S. Host, Suppressor, and Promoter—The Roles of Ni and Fe on Oxygen Evolution Reaction Activity and Stability of NiFe Alloy Thin Films in Alkaline Media. *ACS Catal.* **2021**, *11*, 10537−10552.
(13) Santiago, D.; Cruz-Quiñonez, M.; Tryk, D. A.; Cabrera, C. R. Pt/C Catalyst Preparation Using Rotating Disk-Slurry Electrode (RoDSE) Technique. *ECS Trans.* **2007**, *3*, 35−40.
(14) Santiago, D.; Rodríguez-Calero, G. G.; Rivera, H.; Tryk, D. A.; Scibioh, M. A.; Cabrera, C. R. Platinum Electrodeposition at High Surface Area Carbon Vulcan-XC-72R Material Using a Rotating Disk-Slurry Electrode Technique. *J. Electrochem. Soc.* **2010**, *157*, F189−F195.
(15) Vega-Cartagena, M.; Flores-Vélez, E. M.; Colón-Quintana, G. S.; Blasini Pérez, D. A.; De Jesús, M. A.; Cabrera, C. R. Silver-Palladium Electrodeposition on Unsupported Vulcan XC-72R for Oxygen Reduction Reaction in Alkaline Media. *ACS Appl. Energy Mater.* **2019**, *2*, 4664−4673.
(16) Peña-Duarte, A.; Vijapur, S. H.; Hall, T. D.; Hayes, K. L.; Larios-Rodríguez, E.; Del Pilar-Albaladejo, J.; Santiago, M. B.; Snyder, S.; Taylor, J.; Cabrera, C. R. Iron Quantum Dots Electro-Assembling on Vulcan XC-72R: Hydrogen Peroxide Generation for Space Applications. *ACS Appl. Mater. Interfaces* **2021**, *13*, 29585−29601.
(17) Vélez, C. A.; Soto-Pérez, J. J.; Corchado-García, J.; Larios, E.; Fulvio, P. F.; Echegoyen, L.; Cabrera, C. R. Glucose Oxidation Reaction at Palladium-Carbon Nano-Onions in Alkaline Media. *J. Solid State Electrochem.* **2021**, *25*, 207−217.
(18) Vega-Cartagena, M.; Rojas-Pérez, A.; Colón-Quintana, G. S.; Blasini Pérez, D. A.; Peña-Duarte, A.; Larios-Rodríguez, E.; De Jesús, M. A.; Cabrera, C. R. Potential Dependent Ag Nanoparticle Electrodeposition on Vulcan XC-72R Carbon Support for Alkaline Oxygen Reduction Reaction. *J. Electroanal. Chem.* **2021**, *891*, 115242.
(19) Rivera-Vélez, N. E.; Valdez, T.; González, I.; Fachini, E.; Manzo, M.; Cabrera, C. R. Iridium and Ruthenium Electrodeposition at Platinum Nanopowder Using the Rotating Disc Slurry Electrode Technique. *ECS Trans.* **2011**, *35*, 47−55.
(20) Contes-de Jesus, E.; Santiago, D.; Casillas, G.; Mayoral, A.; Magen, C.; José-Yacamán, M.; Li, J.; Cabrera, C. R. Platinum Electrodeposition on Unsupported Single Wall Carbon Nanotubes and Its Application as Methane Sensing Material. *J. Electrochem. Soc.* **2012**, *160*, H98−H104.
(21) Santiago, D.; Rodríguez-Calero, G. G.; Palkar, A.; Barraza-Jimenez, D.; Galvan, D. H.; Casillas, G.; Mayoral, A.; Jose-Yacamán, M.; Echegoyen, L.; Cabrera, C. R. Platinum Electrodeposition on Unsupported Carbon Nano-Onions. *Langmuir* **2012**, *28*, 17202−17210.
(22) Cunci, L.; Velez, C. A.; Perez, I.; Suleiman, A.; Larios, E.; José-Yacamán, M.; Watkins, J. J.; Cabrera, C. R. Platinum Electrodeposition at Unsupported Electrochemically Reduced Nanographene Oxide for Enhanced Ammonia Oxidation. *ACS Appl. Mater. Interfaces* **2014**, *6*, 2137−2145.
(23) Suleiman, A.; Menéndez, C. L.; Polanco, R.; Fachini, E. R.; Hernández-Lebrón, Y.; Guinel, M. J.-F.; Roque-Malherbe, R.; Cabrera, C. R. Rotating Disk Slurry Electrodeposition of Platinum at Y-Zeolite/Carbon Vulcan XC-72R for Methanol Oxidation in Alkaline Media. *RSC Adv.* **2014**, *5*, 7637−7646.
(24) Vélez, C. A.; Corchado-García, J.; Rojas-Pérez, A.; Serrano-Alejandro, E. J.; Santos-Homs, C.; Soto-Pérez, J. J.; Cabrera, C. R. Manufacture of Pd/Carbon Vulcan XC-72R Nanoflakes Catalysts for Ethanol Oxidation Reaction in Alkaline Media by RoDSE Method. *J. Electrochem. Soc.* **2017**, *164*, D1015−D1021.
(25) Betancourt, L. E.; Guzmán-Blas, R.; Luo, S.; Stacchiola, D. J.; Senanayake, S. D.; Guinel, M.; Cabrera, C. R. Rotating Disk Slurry Au Electrodeposition at Unsupported Carbon Vulcan XC-72 and Ce^{3+} Impregnation for Ethanol Oxidation in Alkaline Media. *Electrocatalysis* **2017**, *8*, 87−94.
(26) Betancourt, L. E.; Ortiz-Rodríguez, Á. M.; Corchado-García, J.; Cabrera, C. R. RoDSE Synthesized Fine Tailored Au Nanoparticles from $Au(X)_4^-$ (X = Cl^-, Br^-, and OH^-) on Unsupported Vulcan XC-72R for Ethanol Oxidation Reaction in Alkaline Media. *ACS Appl. Energy Mater.* **2019**, *2*, 287−297.
(27) Ze, H.; Chen, X.; Wang, X.-T.; Wang, Y.-H.; Chen, Q.-Q.; Lin, J.-S.; Zhang, Y.-J.; Zhang, X.-G.; Tian, Z.-Q.; Li, J.-F. Molecular Insight of the Critical Role of Ni in Pt-Based Nanocatalysts for Improving the Oxygen Reduction Reaction Probed Using an In Situ SERS Borrowing Strategy. *J. Am. Chem. Soc.* **2021**, *143*, 1318−1322.
(28) Xiong, Y.; Yang, Y.; DiSalvo, F. J.; Abruña, H. D. Synergistic Bimetallic Metallic Organic Framework-Derived Pt−Co Oxygen Reduction Electrocatalysts. *ACS Nano* **2020**, *14*, 13069−13080.
(29) Wang, F.; Zhang, Q.; Rui, Z.; Li, J.; Liu, J. High-Loading Pt−Co/C Catalyst with Enhanced Durability toward the Oxygen Reduction Reaction through Surface Au Modification. *ACS Appl. Mater. Interfaces* **2020**, *12*, 30381−30389.
(30) Kim, H. Y.; Kwon, T.; Ha, Y.; Jun, M.; Baik, H.; Jeong, H. Y.; Kim, H.; Lee, K.; Joo, S. H. Intermetallic PtCu Nanoframes as Efficient Oxygen Reduction Electrocatalysts. *Nano Lett.* **2020**, *20*, 7413−7421.
(31) Pérez-Rodríguez, S.; Pastor, E.; Lázaro, M. J. Electrochemical Behavior of the Carbon Black Vulcan XC-72R: Influence of the Surface Chemistry. *Int. J. Hydrogen Energy* **2018**, *43*, 7911−7922.

https://doi.org/10.1021/acsaem.2c02843
ACS Appl. Energy Mater. 2022, 5, 15175−15187

(32) Rolison, D. R. Catalytic Nanoarchitectures - The Importance of Nothing and the Unimportance of Periodicity. *Science* **2003**, *299*, 1698−1701.
(33) Swider, K. E.; Rolison, D. R. The Chemical State of Sulfur in Carbon-Supported Fuel-Cell Electrodes. *J. Electrochem. Soc.* **1996**, *143*, 813−819.
(34) Milazzo, R. G.; Privitera, S. M. S.; D'Angelo, D.; Scalese, S.; Di Franco, S.; Maita, F.; Lombardo, S. Spontaneous Galvanic Displacement of Pt Nanostructures on Nickel Foam: Synthesis, Characterization and Use for Hydrogen Evolution Reaction. *Int. J. Hydrogen Energy* **2018**, *43*, 7903−7910.
(35) Lázaro, M. J.; Calvillo, L.; Celorrio, V.; Pardo, J. I.; Perathoner, S.; Moliner, R.Study and Applications of Carbon Black Vulcan XC-72R in Polymeric Electrolyte Fuel Cells. In *Carbon Black: Production, Properties, and Uses Chemical engineering methods and technology Materials Science and Technologies Series*; Sanders, I. J.; Peeten, T. L., Ed.; NOVA Science Publishers, 2011.
(36) Mcbreen, J.; Olender, H.; Srinivasan, S.; Kordesch, K. V. Carbon Supports for Phosphoric Acid Fuel Cell Electrocatalysts : Alternative Materials and Methods of Evaluation. *J. Appl. Electrochem.* **1981**, *11*, 787−796.
(37) Elgrishi, N.; Rountree, K. J.; McCarthy, B. D.; Rountree, E. S.; Eisenhart, T. T.; Dempsey, J. L. A Practical Beginner's Guide to Cyclic Voltammetry. *J. Chem. Educ.* **2018**, *95*, 197−206.
(38) O'Grady, W. E.; Hagans, P. L.; Pandya, K. I.; Maricle, D. L. Structure of Pt/Ru Catalysts Using X-Ray Absorption Near Edge Structure Studies. *Langmuir* **2001**, *17*, 3047−3050.
(39) Frenkel, A. I. Applications of Extended X-Ray Absorption Fine-Structure Spectroscopy to Studies of Bimetallic Nanoparticle Catalysts. *Chem. Soc. Rev.* **2012**, *41*, 8163−8178.
(40) Ravel, B.; Newville, M. ATHENA, ARTEMIS, HEPHAESTUS: Data Analysis for X-Ray Absorption Spectroscopy Using IFEFFIT. *J. Synchrotron Radiat.* **2005**, *12*, 537−541.
(41) Timoshenko, J.; Roldan Cuenya, B. In Situ/Operando Electrocatalyst Characterization by X-Ray Absorption Spectroscopy. *Chem. Rev.* **2021**, *121*, 882−961.
(42) Soto-Pérez, J.; Betancourt, L. E.; Trinidad, P.; Larios, E.; Rojas-Pérez, A.; Quintana, G.; Sasaki, K.; Pollock, C. J.; Debefve, L. M.; Cabrera, C. R. In Situ X-Ray Absorption Spectroscopy of PtNi-Nanowire/Vulcan XC-72R under Oxygen Reduction Reaction in Alkaline Media. *ACS Omega* **2021**, *6*, 17203−17216.
(43) Alfantazi, A. M.; Ahmed, T. M.; Tromans, D. Corrosion Behavior of Copper Alloys in Chloride Media. *Mater. Des.* **2009**, *30*, 2425−2430.
(44) Hamidah, I.; Solehudin, A.; Hamdani, A.; Hasanah, L.; Khairurrijal, K.; Kurniawan, T.; Mamat, R.; Maryanti, R.; Nandiyanto, A. B. D.; Hammouti, B. Corrosion of Copper Alloys in KOH, NaOH, NaCl, and HCl Electrolyte Solutions and Its Impact to the Mechanical Properties. *Alexandria Eng. J.* **2021**, *60*, 2235−2243.
(45) Seghiouer, A.; Chevalet, J.; Barhoun, A.; Lantelme, F. Electrochemical Oxidation of Nickel in Alkaline Solutions: A Voltammetric Study and Modelling. *J. Electroanal. Chem.* **1998**, *442*, 113−123.
(46) Arkam, C.; Bouet, V.; Gabrielli, C.; Maurin, G.; Perrot, H. Quartz Crystal Electrogravimetry with Controlled Hydrodynamics: Applications to the Study of Nickel Electrodeposition. *J. Electrochem. Soc.* **1994**, *141*, L103−L105.
(47) Jia, Q.; Zhao, Z.; Cao, L.; Li, J.; Ghoshal, S.; Davies, V.; Stavitski, E.; Attenkofer, K.; Liu, Z.; Li, M.; Duan, X.; Mukerjee, S.; Mueller, T.; Huang, Y. Roles of Mo Surface Dopants in Enhancing the ORR Performance of Octahedral PtNi Nanoparticles. *Nano Lett.* **2018**, *18*, 798−804.
(48) Giri, S. D.; Sarkar, A. Electrochemical Study of Bulk and Monolayer Copper in Alkaline Solution. *J. Electrochem. Soc.* **2016**, *163*, H252−H259.
(49) Oshchepkov, A. G.; Braesch, G.; Bonnefont, A.; Savinova, E. R.; Chatenet, M. Recent Advances in the Understanding of Nickel-Based Catalysts for the Oxidation of Hydrogen-Containing Fuels in Alkaline Media. *ACS Catal.* **2020**, *10*, 7043−7068.
(50) Briega-Martos, V.; Herrero, E.; Feliu, J. M. Effect of PH and Water Structure on the Oxygen Reduction Reaction on Platinum Electrodes. *Electrochim. Acta* **2017**, *241*, 497−509.
(51) Shinagawa, T.; Garcia-Esparza, A. T.; Takanabe, K. Insight on Tafel Slopes from a Microkinetic Analysis of Aqueous Electrocatalysis for Energy Conversion. *Sci. Rep.* **2015**, *5*, 13801.
(52) Murthi, V. S.; Urian, R. C.; Mukerjee, S. Oxygen Reduction Kinetics in Low and Medium Temperature Acid Environment: Correlation of Water Activation and Surface Properties in Supported Pt and Pt Alloy Electrocatalysts. *J. Phys. Chem. B* **2004**, *108*, 11011−11023.
(53) Zinola, C. F.; Castro Luna, A. M.; Triaca, W. E.; Arvia, A. J. Kinetics and Mechanism of the Electrochemical Reduction of Molecular Oxygen on Platinum in KOH: Influence of Preferred Crystallographic Orientation. *J. Appl. Electrochem.* **1994**, *24*, 531−541.
(54) Tammeveski, K.; Arulepp, M.; Tenno, T.; Ferrater, C.; Claret, J. Oxygen Electroreduction on Titanium-Supported Thin Pt Films in Alkaline Solution. *Electrochim. Acta* **1997**, *42*, 2961−2967.
(55) Yang, Y.; Chen, G.; Zeng, R.; Villarino, A. M.; DiSalvo, F. J.; van Dover, R. B.; Abruña, H. D. Combinatorial Studies of Palladium-Based Oxygen Reduction Electrocatalysts for Alkaline Fuel Cells. *J. Am. Chem. Soc.* **2020**, *142*, 3980−3988.
(56) Han, X.-F.; Batool, N.; Wang, W.-T.; Teng, H.-T.; Zhang, L.; Yang, R.; Tian, J.-H. Templated-Assisted Synthesis of Structurally Ordered Intermetallic Pt_3Co with Ultralow Loading Supported on 3D Porous Carbon for Oxygen Reduction Reaction. *ACS Appl. Mater. Interfaces* **2021**, *13*, 37133−37141.

https://doi.org/10.1021/acsaem.2c02843
ACS Appl. Energy Mater. 2022, 5, 15175−15187